Ignition and behavior of arc spots on helium irradiated tungsten under fusion relevant condition

Shin Kajita
Institute of Materials and Systems for Sustainability
Nagoya University
Nagoya, Japan
kajita.shin@nagoya-u.jp

2nd Dogyun Hwangbo
Graduate School of Engineering
Nagoya University
Nagoya, Japan

3rd Noriyasu Ohno
Graduate School of Engineering
Nagoya University
Nagoya, Japan

***Abstract*—In nuclear fusion reactors, unipolar arcing is a longstanding plasma surface interaction issue. In this paper, short summaries of morphology changes by helium plasma irradiation under fusion relevant conditions and ignition of arcing on the He irradiated surfaces are given. Helium plasma irradiation leads to surface morphology changes, and arcing can be ignited on the surface in response to pulsed heat load accompanied by plasma instabilities. Then, we focused on arcing ignited on large-scale fiberform nanostructures (LFNs) formed with deposition of metallic particles together with helium ion irradiation. Dusts releases from the arc spot and the amount of material erosion are discussed based on the experiments.**

***Index Terms*—unipolar arc, nuclear fusion, helium plasma induced nanostructures**

I. Introduction

Material erosion by unipolar arcing, which has been regarded as important phenomenon in nuclear fusion devices [1], [2], could lead to damages of plasma facing components and deterioration of the plasma performance. When the limiter configuration was used in 1970-80's, it was thought that arcing was one of the major impurity sources [3]; since the divertor configuration was adapted, sputtering was regarded to dominate the erosion by arcing. However, arcing has been reported again in the last ten years from various fusion devices including ASDEX upgrade [4]–[7], the large helical device (LHD) [8], DIII-D [9]–[11], and JT-60U [12]. At the moment, tungsten (W) is the most promising material for plasma facing componetnts in terms of the material erosion, tritium retention and so on. Since the radiation power from W can be three orders magnitude greater than that from carbon when the impurity level is the same [13], the amount of W erosion is a crucial issue.

It is likely that the following two major factors lead to the revival of arcing in fusion devices: transient heat/particle loads on materials [14] and surface roughening by the plasma irradiation [15]. In the high confinement H-mode, Edge Localized Mode of instability (ELMs) results in the observation of short bursts of the core plasmas [13]. Especially, among three types of ELMs (type I-III), type-I (giant) ELMs will provide high pulsed heat/particle loads, typically $\sim$1 MJ/m^2 during 0.1-1 ms. Results in ASDEX upgrade [5] and DIII-D [11] suggested that the timings of arcing were correlated with ELM events.

In fusion devices, plasma facing components will be subjected to ions of hydrogen isotopes, helium, which can be formed by nuclear fusion reactions, and some impurities. Bombardments of these ions to metal surface lead to various surface morphology changes. Accumulation of hydrogen isotopes in a small void increases the pressure inside metals and form blisters [16], which can lead to cracking, exfoliation, and dust formation. In divertor region in fusion reactors, the concentration of He ions can be up to 10 %.

When certain set of conditions are satisfied (the surface temperature of 1000-2000 K and the incident ion energy higher than $\sim$30 eV [17]), fiberform nanostructures (FNs) called *fuzz* are grown on the surface by the He plasma irradiation [18], [19]. Because the thermophysical properties of the surface layer are altered significantly, thermal response could be radically changed by the existence of the FNs [20], [21]. Unipolar arcing was prone to be ignited on the nanostructured layers, as was demonstrated in linear devices [15], [22], [23], LHD [8], and DIII-D [10].

In this paper, we focused on arcing initiated on W exposed to He plasmas, which probably lead to the most influential damages for arcing on plasma facing components. After short review of the He irradiation effects and arc spot formation on W exposed to He plasmas, we show experiments on the samples with large-scale fiberform nanostructures (LFNs), which may be formed under fusion relevant conditions. Previously, it was shown that arcing can be ignited also on LFNs and dusts can be formed on the arc spots initiated [24]. In this study, detailed ehaviors of arc spots and material erosion by arcing on the LFNs are revealed.

II. Helium plasma induced nanostructures

A. Fuzzy nanostructures

In Fig. 1, scanning electron microscope (SEM) micrographs of W sample exposed to a He plasma are shown. The linear plasma NAGDIS (Nagoya divertor simulator) devices, which can produce steady state arc discharges using a heated LaB_6 cathode, were used for the the plasma irradiation. The substrate temperature, which is increased by the heat flux from the plasma, can be above 1500 K without an active heating.

He atoms are easily trapped in metals, different from hydrogen and hydrogen isotopes, because He atoms are more

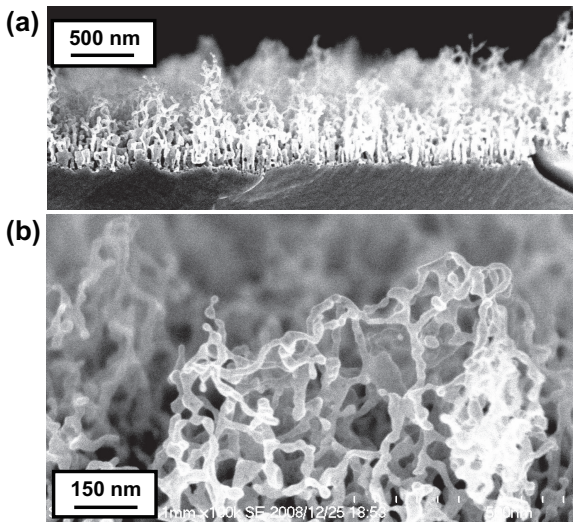

Fig. 1. Cross sectional SEM micrographs of fiberform nanostructured W. The surface temperature during the irradiation, incident ion energy and helium fluence are 1700K, ∼50 eV, and 2×10^{26} m^{-2}, respectively. The helium irradiation was performed in the NAGDIS-I. (from [25] Copyright 2018 The Japan Society of Applied Physics)

stable in metals. Although the penetration depth of He atoms to W surface is in average ∼3 nm when the incident ion energy is lower than 100 eV [26], He atoms are diffused in W matrix to much deeper region than the initial penetration depth [27]. The increase in the concentration of He atoms results in the formation of He clusters and He bubbles, which lead to growth of protrusions on the surface. Detailed transmission electron microscope (TEM) analysis revealed that the growths of protrusions by swelling process are involved in the formation of FNs at least in the initial phase [28].

The thickness of the FN layer grew in proportional to the square root of the irradiation time [19], [29], indicating that the growth was controlled by some diffusion process. Typically, He fluence of 5×10^{25} m^{-2} is necessary for the FNs to fully cover the surface. FNs in the same feature can be grown on other metals including molybdenum, tantalum, iron, nickel, rhenium, rhodium, platinum, and ruthenium [30]–[34].

It is still an open question whether fuzz growth occurs in actual fusion devices. The incident ion energy would be lower than the threshold energy of 30 eV in fully detached plasmas or around strike point in partially detached plasmas. However, the ion energy could be greater than 30 eV during ELMs. Yu *et al.* simulated transient heating events using a pulsed laser [35]. Fuzz growth was enhanced considerably due to a cyclic transient heating, and the fuzz thickness was ∼10 times thicker than theoretical model. On the other hand, when the temperature of fuzzy surface was increased without sufficient He flux, the nanostructures were reintegrated to the surface, and fine structures were annealed out [36], [37]. As was recently investigated by De Temmerman *et al.* [38], considering the enhanced growth during ELMs and the annealing effects, it was shown that thin (<2 μm thick) fuzzy layer can be grown in ITER when the ELM heat load is small. Another factor that should be considered further is the effect of deposition, as will be discussed later.

When FNs are formed on the surface, physical properties of the surface are changed. It was revealed that the porosity, which was measured from the mass measurement and SEM observation, increased with increasing the FN layer thickness, and it became ∼90% when the FN layer was 1 μm thick [39]. Moreover, a TEM analysis demonstrated that top part of the nanostructured layer has a higher porosity [40]. The effective surface area also increases with increasing the porosity. Brunauer, Emmet and Teller (B.E.T.) method measured 27 times higher effective surface area when the fuzzy layer thickness was ∼3 μm [41]. The field electron emission started to be observed much lower electric field, typically 10 kV/mm, on the surface with FNs. Also, the field electron emission current increased after He plasma irradiation due to surface roughness with He bubbles and FNs [42]. The field enhancement factor, deduced from Fowler-Nordheim plot, was higher (∼1000) than that on flat surfaces.

Thermophysical properties are important factors for the plasma material interaction. Because the layer with He induced damages is not so thick, typically less than μm, the impact on the steady state heat load is not altered by the variation in the thermal conductivity, whereas the influence of transients can be changed. The thermal conductivity of Cu ion-irradiated W was measured using 3Ω method; the thermal conductivity was decreased by approximately 60% [43]. The Cui *et al.* used the method for He irradiated W. The thermal conductivity was decreased by an order of magnitude on the He irradiated layer [44]. A thermoreflectance method was applied to fuzzy W layer, and the thermal conductivity, which was measured from the heat diffusion across the layer, was less than 1% of bulk value [45]. However, temperature increases in response to plasma and laser pulses on the FN sample suggested a much greater decrease in the thermal conductivity, presumably due to height dependence of the porosity and/or existances of thermally isolated part [21].

B. Large scale fiberform nanostructure

Isolated nanostructured tendril bundles (NTBs) have been found on the irradiation in the DIONISOS experimental device which used RF He plasma source at a frequency of 13.56 MHz. The height reached ∼30 μm, and it was discussed that ion energy modulation provided a new parameter to control the morphology [46]. Hwangbo *et al.* revealed that NTB growth occurred when small amount of impurity (Ar, Ne, N_2) was injected to He plasmas [47], suggesting that sputtered W atoms were contributed to the growth of NTBs. Figure 2(a) shows an SEM micrograph of the NTB formed in the NAGDIS-II device.

Recent experiments revealed that an additional precipitation of metallic particles during helium plasma irradiation changed the growth rate completely. Fuzzy fur structures with 1 mm-thick visible tungsten and molybdenum covered a tungsten metal substrate in an hour of irradiation [48], [49]. The results suggested that additional precipitation of metallic ions breaks

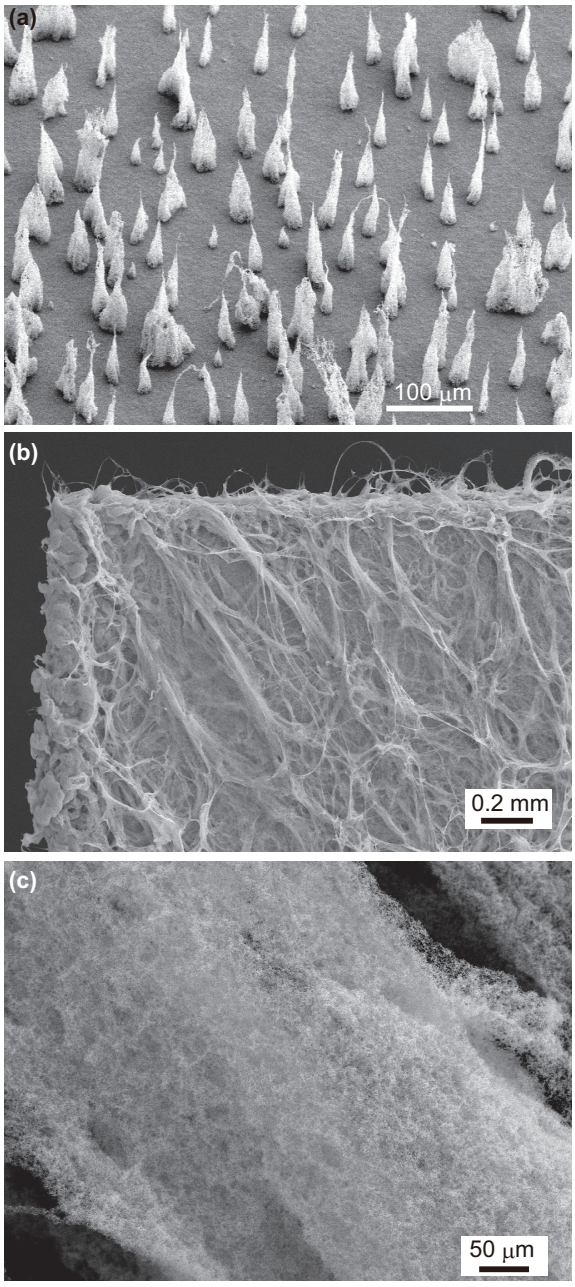

Fig. 2. (a) An SEM micrograph of the NTB formed in the NAGDIS-II device with an introduction of small amount of impurity (N_2) and (b,c) SEM micrographs of W large scale fiberform nanostructures grown on W sample.

the bottleneck diffusion process. Figures 2(b,c) show SEM micrographs of W large scale fiberform nanostructures (LFNs) grown on W sample. A sputtering wire (W), which was biased negatively high enough to initiate sputtering, was installed adjacent to a substrate. The substrate was exposed to W particles, which was released from the sputtering wire and ionized before reaching the substrate together with He ions. It is seen in Fig. 2(b) that nanostructures greater than 100 μm were grown from the edge of the sample and fine structures covered the surface; FNs comprised the LFNs, as shown in Fig. 2(c). The growth rate of the fuzzy structures became orders of magnitude greater than conventional fuzz growth when precipitating W particles. In fusion devices, because re-deposition of sputtered atoms can occur in deposition dominant locations, there is a possibility that the enhanced growth of FN occurs.

III. Unipolar arcing on fiberform nanostructures

A. Ignition condition

Arcing is easily ignited on the nanostructured W surfaces in response to transients. Ignitions were confirmed in response to laser pulses [15] and pulsed plasmas [23], [50]. Even a steady state plasma exposure ignited arcing in the large helical device [8]. Noteworthy is that arcing was ignited even when the target was at the floating potential, where no power was supplied from a power supply; the power should be supplied from the surrounding plasma. Nanostructured surface realized the direct observation of unipolar arcing in laboratory experiments probably for the first time [15]. The surface morphology changes significantly alter the ignition property. This would be mainly because of the decrease in the thermal conductivity and t increase in the field emission current, as was described in the last section. The ignition process of the unipolar arcing on nanostructured W was modeled using an explosive emission (ecton) mechanism [51]. It was revealed from systematic experiments that the target potential was an important factor to initiate and sustain the arcing [52]. No arcing was observed when the target potential was higher than -50 V. Considering that the fact that the measured space potential by an electrostatic probe was $\sim$-5 V, the potential of the target corresponded to $\sim$-45 V to the plasma. Similar dependence in the target potential was identified on the arcs initiated in response to pulsed plasmas [23].

B. Behavior of arc spots

Figures 3(a,b) show SEM micrographs of an arc trail formed on a nanostructured W surface. The arc spots moved in a random manner locally, but it moved to a specific direction following the acute angle rule and retrograde motion [53], because of an influence of magnetic field. It is known that arc trails have fractal features [53], and arc trails recorded on fuzzy W also had a clear fractal pattern. A fractal dimension analysis using a box counting method measured a high local fractal dimension (1.5–2.0) and a low global fractal dimension ($\sim$1.0), suggesting that the trail has a self-affine fractality [54]. The fractality altered when changing the magnetic field strength especially in the range of 0.05-0.5 T [55]. Moreover, the fractal dimension was altered when the arc spots formed a group [56], and the grouping feature could be altered by the thickness of the fuzzy layer.

The plasma parameters of arc spots formed on the nanostructured W was characterized by Hwangbo *et al.* and Aussems *et al.* using spectroscopic methods [57], [58]. The temperature was deduced from the Boltzmann plot method, and the density was deduced from the Saha-Boltzmann equation. The electron temperature and density of the arc spots were in the range 0.5–0.85eV and 0.7–2.0$\times 10^{20}$ m^{-3}, respectively.

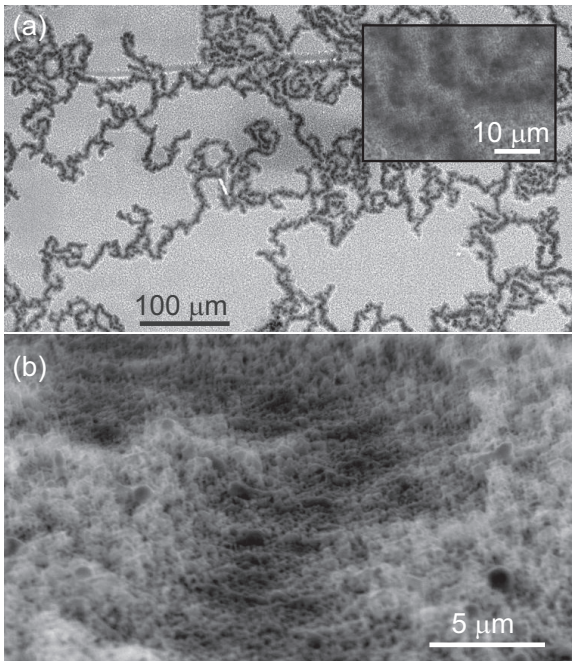

Fig. 3. SEM micrographs of arc trails on nanostructured W surface at different magnifications.

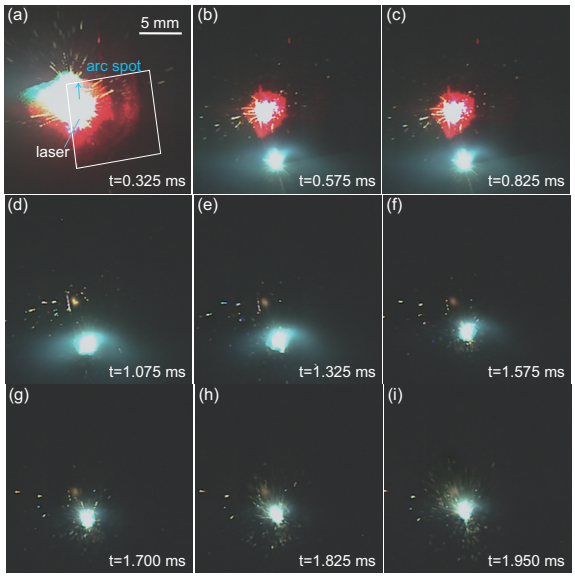

Fig. 4. Fast framing camera images of arc spots initiated from the laser irradiated spots on LFN sample.

C. Material erosion

The erosion of material was estimated from the cross-sectional transmission electron microscopy (TEM) micrograph of arc trails. It was roughly assessed that W eroded by arcing was 10 mg/s [52]. The erosion rate was systematically investigated from the mass loss measurements of samples after arcing [59]. The erosion rate increased with the averaged arc current (4-12 A) from 4 to 10 mg/s, but the erosion per charge did not have a clear current dependence and was in the range of 0.5-1.1 mg/C. The erosion rate was assessed to be 10-30 mg/s in a different device at an averaged arc current of $\sim$20 A in [22]; the value was consistent with that in the NAGDIS-II experiments in terms of the erosion per charge. However, the erosion per charge increased from 0.5 to 1.6 mg/C with increasing the fuzzy layer thickness from 1 to 3 μm, suggesting that the dust release enhanced the erosion rate [60].

IV. Arcing on large-scale nanostructures

A. Observation of arc spots and dusts release

Arc ignition experiments on W substrates with LFNs were conducted in the NAGDIS-II device. The size of the sample was 10$\times$10 mm. The samples with the LFNs were prepared while defining the formation conditions presented previously [48], [49], and conditions were different by samples. All of the samples had visible LFNs in a rather large area, although the amount of LFNs differed by samples. The sample surface temperature, the incident ion energy, the irradiation time, the biasing of sputtering wire used for the experiments were in the ranges of 1210-1440 K, 55-110 eV, 1800-3600 s, and -300 $-$ -500 V. Arcing was ignited using a laser pulse with the pulse width of 0.6 ms in the same manner as in a previous study [52]. The sample was biased to -90 V before the ignition of arcing, and the maximum current was limited by a power supply (5-20 A). The magnetic field strength was 0.1 T. The arcing was ignited approximately twice on the same sample with an interval of typically one min, and the probability of the ignition was almost 100%. We measured mass loss from the mass change of the sample after the series of experiments. Although erosion rate could be differed for the first and second arcs, we used averaged values in this study.

Figure 4(a-i) shows images of the fast framing camera observation at different times. At 0.325 s, an arc spot was initiated from the laser irradiated point and started to move upward, which corresponds to the retrograde direction. Many glowing particles are released from the bright area which corresponds to laser irradiated point and arc spot. The arc spot moved to the backside when it reached the top of the sample and appeared on the front side again at 0.575 ms. The strong emission region was approximately 2 mm in diameter, and there was a larger plume, roughly five times greater, outside the strong emission region. The arc spot started to release many glowing particles from $\sim$1.6 ms like fireworks, indicating that heated dusts or droplets were released from the arc spot.

Figure 5 shows the speeds of arc spots measured from the fast framing camera images on three different samples (sample 1-3). The speed of the spot initiated on sample 1 was $\sim$20 m/s, and the spot rotated four times in 3.5 ms, while the spot speed on samples 2-3 was slower. In average the speed was $\sim$9.8 and 7.1 m/s for sample 2 and 3, respectively. Since the conditions of the plasma were the same, the results indicated that the surface nature changed the spot speed. It is noted that the spot speed on LFNs was much slower than that on conventional fuzzy layer. Previously, it was shown that the spot speed was dependent on the fuzzy layer thickness [56]. The

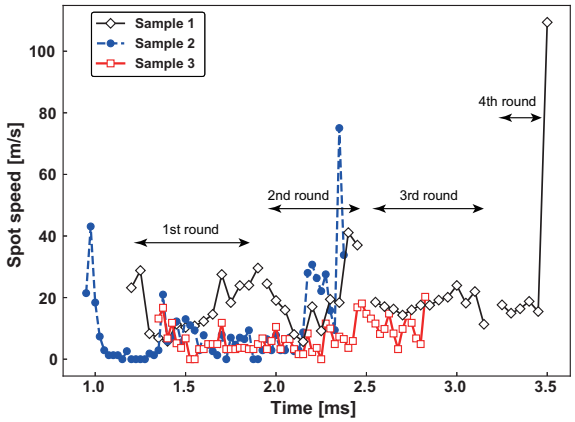

Fig. 5. Spots speed measured from the fast framing camera images.

spot speed was ∼130 and 20 m/s on ∼1 and 5 μm thick fuzz layer samples, respectively, suggesting that the speed could be slower on LFNs compared with that on a 3 μm thick fuzzy sample.

From the fast framing camera images, we can also measure the speed of dusts. Figure 6 shows distribution of the speed of dusts in the parallel direction to the surface from arc spots ignited on samples 1-3. They were measured from the length of the emission line from dusts. As shown in insets in Fig. 6, the dusts were mainly released toward the moving direction of arc spot on sample 1, while they seemed to be released in random direction on samples 2-3. The dust speed was distributed from 20-55 m/s in Fig. 6(a), while it was slower on samples 2 and 3 and was mainly in the range of 8-40 m/s. It was interesting to note that the minimum speed was almost consistent with the spot speed shown in Fig. 5, indicating that the dust speed was influenced by the speed of the spot releasing the dusts.

B. Mass releases

Figures 7(a-d) show the evolutions of the target current and the potential in response to the ignition of arcing on sample 1. In response to the ignition of arcing, jumps in the current and potential were identified. The arc duration was ∼75 ms for the first time, but it was shorter for the second time. Figure 8(a) summarizes the arc durations on eight samples for the first and second times. The duration for the first arc was in the range of 15 to 81 ms, while that for the second arc was in the range of 2 to 21 ms. The duration altered shot by shot, but second arcs were always shorter than first arcs. This was probably because the first arc removed most of the LFNs, and the second arc was terminated at positions where the fuzzy layer has been removed. Figure 8(b) shows averaged arc current for the eight samples including both of the first and second arc events. The current was 13-15 A for sample 1-6, ∼10 A for sample 7, and ∼4 A for sample 8. For sample 8, the current limit was 5 A.

The mass loss by arcing was measured from mass changes of samples with an electronic scale (A&D Co., BM-22), and the erosion rate and the erosion per charge were estimated. Even without arcing, the mass loss was identified, different

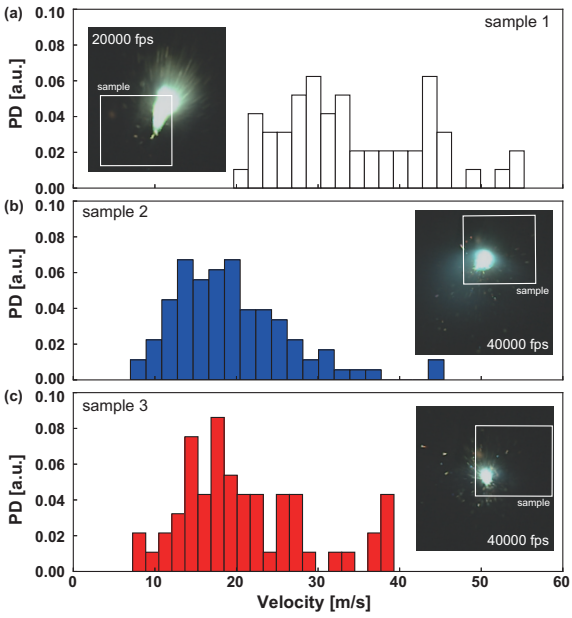

Fig. 6. Distribution of dust's speeds in the parallel direction to the surface from arc spots on samples 1-3.

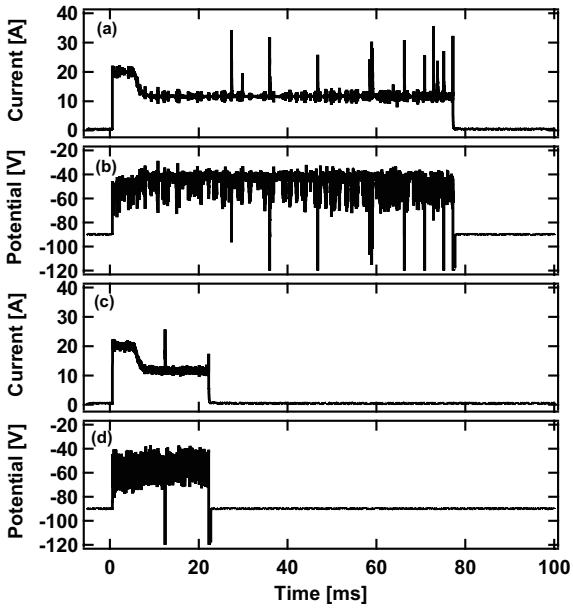

Fig. 7. The evolutions of the (a,c) target current and (b,d) potential in response to the ignition of arcing for sample 1. (a,b) and (c,d) correspond to the first and second arcs, respectively.

from the conventional fuzzy sample [59]; in average, the mass loss by a laser pulse was 0.078 mg/pulse. This indicates that the LFNs can be easily blown off only by laser pulses. The mass loss by laser pulses was subtracted to estimate the mass loss by arcing. Figure 8(c) shows erosion rate calculated from the mass loss and the arc duration for the eight samples. The erosion rate was in the range of 3-12 mg/s except for sample 8, on which the value was less than 1 mg/s. Previously, it was shown that the erosion rate increased with an increase of the

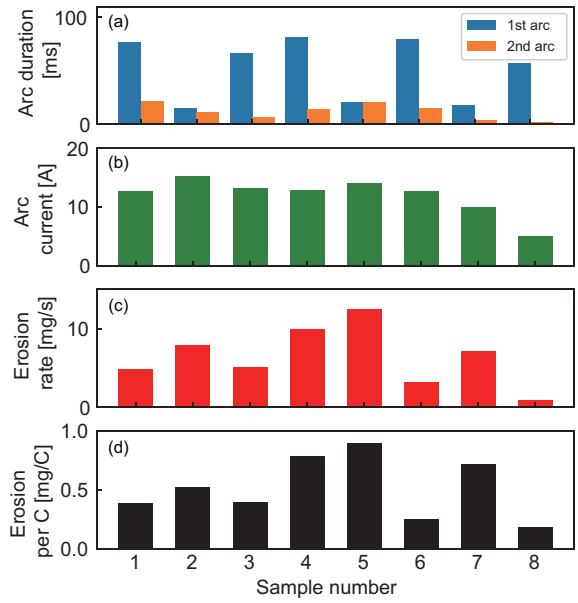

Fig. 8. (a) The arc durations for the first and second times, (b) the averaged arc currents, (c) the erosion rate, and (d) the erosion per charge. The arc experiments were conducted using eight samples. To measure the erosion rate and erosion per charge, the mass loss by laser pulses was measured on a different sample and subtracted.

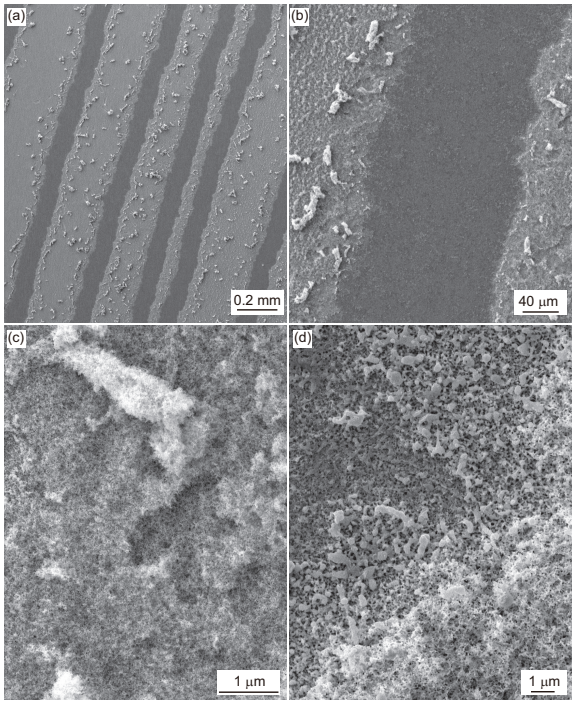

Fig. 9. SEM micrographs of the arc trails

arc current [59] and was ∼4 mg/s even at the arc current of 4 A, which was four to five times greater than the present study. One can say that the erosion rate was not necessarily increased even when the fuzzy layer thickened by orders of magnitude. When the value was converted to erosion per charge, as shown in Fig. 8(d), the value was scattered in the range of 0.2-0.9 mg/C with no clear current dependence. One of the reasons to cause the large scattering was the difference in the LFN amount by samples. Even considering the ambiguity, the value was comparable or lower than that for 2 μm thick fuzzy sample, where the erosion per charge was in the range of 0.5-1.1 mg/C [60]. The results seemed to be contradicted our predictions from the previous results, in which the erosion per charge increased with increasing the fuzzy layer thickness. The lower erosion per charge suggested that the major material erosion was not originated from the highly porous LFNs but from the deposition layer beneath the LFNs. It was likely that the properties of the deposition layer were different from the conventional fuzzy layer or the thickness of the layer was less than 2 μm.

C. Observation of arc trails and collected dusts

Figure 9 shows SEM micrographs of arc trails recorded on sample 8. Straight 0.1 mm width arc trails were seen, and dusts were attached on both sides of the arc trails. The width of 0.1 mm is an order of magnitude greater than that of single arc spot, which has typically the width of 0.01 mm. Figure 9(c) shows an enlarged SEM micrographs of the attached dusts. Those dusts are comprised of fuzzy nanostructures without significant melting, indicating that arcing blew off nanostructures and some were released from and other were reattached to the sample. Figure 9(d) shows an SEM micrographs showing a transition part from the arc trail to nanostructures. The nanostructures were totally melted in the arc trail, and sub-micrometer sized droplets were formed in the edge of the arc trail. On the vicinity of the arc trail, part of the nanostructures was melted, and droplets were attached to the nanostructures.

The trail was quite different from the one shown in Fig. 3. On sample 8, since the current was ∼5 A in average, which was comparable to that shown in Fig. 3, there should be other factors than the arc current. Similar to the discussion in the erosion rate, one of the reasons could be in the fact that the deposition layer could have different material property than conventional fuzzy layer formed by pure He plasma irradiation. Apparently, the trail width was wider than that of a single spot, which was typically 10 μm, suggesting that multiple spot formed a grouping. The layer formed during deposition could have a different porosity, which might have changed the behavior of arc trails including grouping features.

Dusts released from the surface were collected using a copper (Cu) sheet located down below the sample. The color of the Cu sheet was changed in part, indicating that W was evaporated, and a thin film was formed on the sheet by deposition of those atoms. Figure 10 shows SEM micrographs of dusts collected. Many dusts were found on the Cu sheet, as can be seen in Fig. 10(a) as white spots. Figures 10(b-d) show SEM micrographs of dusts, of which the size was less than 0.1 mm. Droplets were observed on the surface and near the dusts, but fine fiberform structures were basically remained.

Red colored square regions in Figs. 10(b-d) are shown in Figs. 11(a-c) with higher resolutions. In Fig. 11(a), it is seen

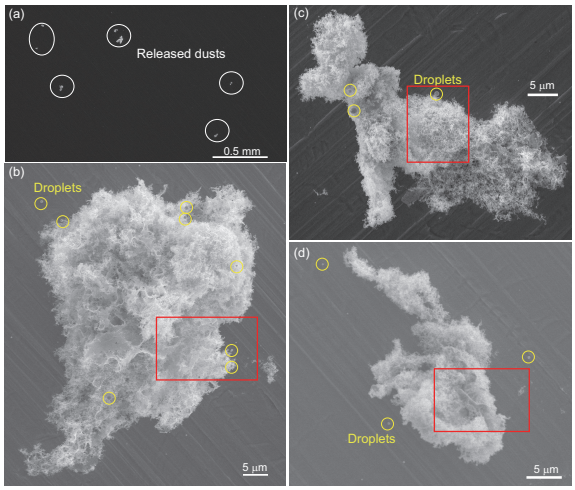

Fig. 10. SEM micrographs of dusts on a Cu sheet located below the arc electrode.

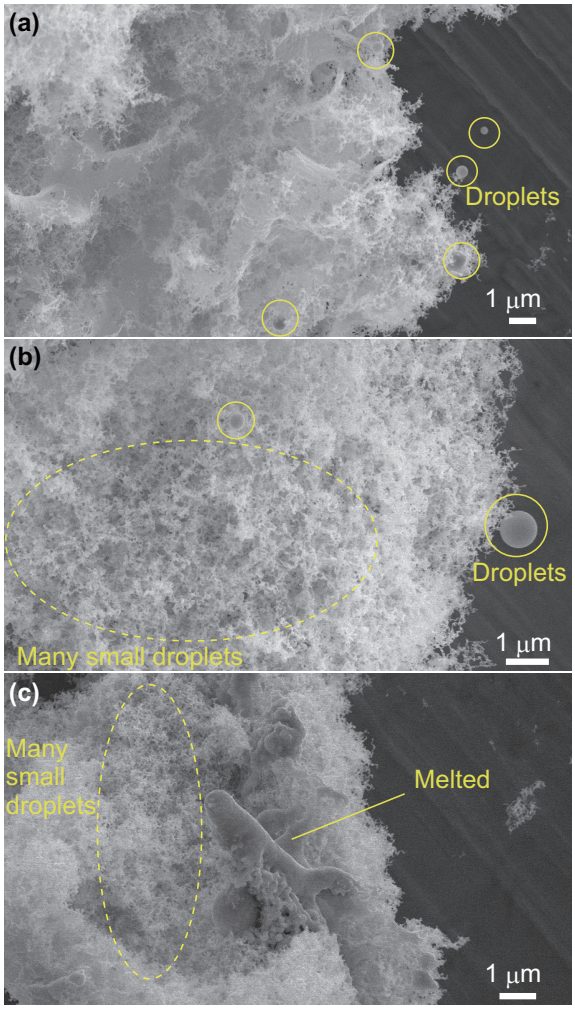

Fig. 11. SEM micrographs of red marked area in Figs. 10(b-d) with higher resolutions.

that dusts are comprised of fiberform and membrane structures, and sub-micrometer droplets are formed on some top part of the fine structures. On the dust shown in Fig. 11(b), a micrometer sized droplet was formed, and, moreover, top of the nanostructures melted, and small 100 nm sized droplets were formed on the nanostructures. In Fig. 11(c), totally melted object was formed, and nanostructures were covered with small droplets in the vicinity of the melted object. The results indicated that some part of the dusts was heated up and melted, but bulk of the dust remained below the melting point. For the dust with the velocity of 10-50 m/s, the small plasma around the arc spot might be transparent. If the plume size is 1 mm and the spot velocity is 20 m/s, the dust can pass through the plume within 50 μs, which may not be enough to fully destroy the dusts. The transportation process of the dust released from the surface could be an important issue in fusion devices. If those dusts entered in the confinement region, it would result in deterioration of the plasma performance and could lead to disruption of plasmas.

V. Conclusions

In fusion devices, plasma irradiations lead to morphology changes, and synergistic effects of the morphology changes with pulsed heat loads accompanied with edge localized modes (ELMs) could results in unipolar arcs. In this study, we focused on helium (He) effects, because they will lead to the most significant morphology changes. It was shown that FNs are grown by He plasma irradiation. The nanostructures could decrease the thermal conductivity and increase the field electron emission current by orders of magnitudes. Moreover, when the deposition occurs on the surface, mm thick large scale fiberform nanostructures (LFNs) can be formed on the surface. In this paper, the He irradiation effects were reviewed and briefly showed behaviors of arcs ignited on conventional FNs.

Then, we showed detailed arcing behaviors on the LFNs. The arc duration was significantly longer on the LFNs for the first time (15-81 ms), but it decreased for the second time, because the LFNs were blown off by the first arcing event. The spot speed was slower than that on the conventional fiberform nanostructures. Dusts were observed to be released from the arc spot, and the speed of the dusts in the parallel direction to the surface was in the range of 10-50 m/s. The minimum speed was almost consistent with the speed of the arc spot. The erosion rate and erosion per charge were in the ranges of 1-12 mg/s and 0.2-0.9 mg/C, respectively. The values were comparable or lower than those on conventional fiberform nanostructures. We collected dusts released from the sample and conducted SEM observation of those dusts. Although melting traces and droplets were found on dusts, they were mainly comprised with fiberform or membrane nanostructures, indicating that released dusts were not easily melted after released from arc spots. For the future work, it is of interest to investigate how those dusts can be transported in plasmas and assess the possibility to enter the core region without sufficient ionizations.

ACKNOWLEDGMENT

The author thanks Mr S. Kawaguchi for preparation of LNF samples, and Prof. S. Takamura and Prof. N. Yoshida for fruitful discussion and their supports. This work was supported in part by a Grant-in-Aid for Scientific Research (B) 15H04229 and (A) 16H02440, and Fund for the Promotion of Joint International Research 17KK0132 from the Japan Society for the Promotion of Science (JSPS), and JSPS Bilateral Joint Research Project. This work is also supported in part by the NINS program of Promoting Research by Networking among Institutions (Grant Number 01411702).

REFERENCES

[1] R. Behrisch, *Physics of Plasma-Wall Interactions in Controlled Fusion (Nato ASI Series, Series B, Physics)* (Plenum Pub. Corp., 1986), pp. 495–513.
[2] G. Federici, C. Skinner, J. Brooks, J. Coad, C. Grisolia, A. Haasz, A. Hassanein, V. Philipps, C. Pitcher, J. Roth, W. Wampler and D. Whyte: Nucl. Fusion **41** (2001) 1967.
[3] G. McCracken and P. Stott: Nuclear Fusion **19** (1979) 889.
[4] A. Herrmann, M. Balden, M. Laux, K. Krieger and H. M Journal of Nuclear Materials **390-391** (2009) 747.
[5] V. Rohde, N. Endstrasser, U. Toussaint, M. Balden, T. Lunt, R. Neu, A. Hakola and J. Bucalossi: Journal of Nuclear Materials **415** (2011) S46.
[6] V. Rohde, M. Balden, N. Endstrasser and U. von Toussaint: Journal of Nuclear Materials **438** (2013) S800.
[7] V. Rohde and M. Balden: Nuclear Materials and Energy **9** (2016) 36.
[8] M. Tokitani, S. Kajita, S. Masuzaki, Y. Hirahata, N. Ohno, T. Tanabe and LHD Experiment Group: Nucl. Fusion **51** (2011) 102001.
[9] D. Rudakov, C. Chrobak, R. Doerner, S. Krasheninnikov, R. Moyer, K. Umstadter, W. Wampler and C. Wong: Journal of Nuclear Materials **438** (2013) S805.
[10] D. L. Rudakov *et al.*: Physica Scripta **2016** (2016) 014055.
[11] I. Bykov, C. P. Chrobak, T. Abrams, D. L. Rudakov, E. A. Unterberg, W. R. Wampler, E. M. Hollmann, R. A. Moyer, J. A. Boedo, B. Stahl, E. T. Hinson, J. H. Yu, C. J. Lasnier, M. Makowski and A. G. McLean: Physica Scripta **2017** (2017) 014034.
[12] S. Kajita, M. Fukumoto, M. Tokitani, T. Nakano, Y. Noiri, N. Ohno, S. Masuzaki, S. Takamura, N. Yoshida and Y. Ueda: Nuclear Fusion **53** (2013) 053013.
[13] J. Wesson, *Tokamaks* 4th ed. (Oxford Science Publications, Oxford, 2011).
[14] M. Laux, W. Schneider, B. Jüttner, M. Balden and S. Lindig: IEEE Transactions on Plasma Science **33** (2005) 1470.
[15] S. Kajita, S. Takamura and N. Ohno: Nucl. Fusion **49** (2009) 032002.
[16] Y. Ueda, T. Funabiki, T. Shimada, K. Fukumoto, H. Kurishita and M. Nishikawa: Journal of Nuclear Materials **337-339** (2005) 1010 , pSI-16.
[17] S. Kajita, W. Sakaguchi, N. Ohno, N. Yoshida and T. Saeki: Nucl. Fusion **49** (2009) 095005.
[18] S. Takamura, N. Ohno, D. Nishijima, and S. Kajita: Plasma Fusion Research **1** (2006) 051.
[19] M. Baldwin and R. Doerner: Nucl. Fusion **48** (2008) 035001 (5pp).
[20] S. Kajita, N. Ohno, W. Sakaguchi and M. Takagi: Plasma Fusion Research **004** (2000) 004.
[21] S. Kajita, G. D. Temmerman, T. Morgan, S. van Eden, T. de Kruif and N. Ohno: Nuclear Fusion **54** (2014) 033005.
[22] D. Aussems, D. Nishijima, C. Brandt, H. van der Meiden, M. Vilemova, J. Matejicek, G. D. Temmerman, R. Doerner and N. L. Cardozo: Journal of Nuclear Materials **463** (2014) 303.
[23] M. Yajima, N. Ohno, S. Kajita, G. D. Temmerman, K. Bystrov, S. Bardin, T. Morgan and S. Masuzaki: Fusion Engineering and Design **112** (2016) 156 .
[24] S. Kajita, *2018 28th International Symposium on Discharges and Electrical Insulation in Vacuum (ISDEIV)* (2018), Vol. 1, pp. 1–6.
[25] S. Kajita, T. Saeki, Y. Hirahata, M. Yajima, N. Ohno, R. Yoshihara and N. Yoshida: Jpn. J. Appl. Phys. **50** (2011) 08JG01.
[26] W. Eckstein: IPP (2002) 9/132.
[27] S. Kajita, N. Yoshida, R. Yoshihara, N. Ohno and M. Yamagiwa: Journal of Nuclear Materials **418** (2011) 152.
[28] S. Kajita, N. Yoshida, N. Ohno and Y. Tsuji: New Journal of Physics **17** (2015) 043038.
[29] T. Petty, M. Baldwin, M. Hasan, R. Doerner and J. Bradley: Nuclear Fusion **55** (2015) 093033.
[30] S. Kajita, T. Yoshida, D. Kitaoka, R. Etoh, M. Yajima, N. Ohno, H. Yoshida, N. Yoshida and Y. Terao: Journal of Applied Physics **113** (2013) 134301.
[31] S. Takamura and Y. Uesugi: Applied Surface Science **356** (2015) 888.
[32] S. Kajita, T. Ishida, N. Ohno, D. Hwangbo and T. Yoshida: Sci. Rep. **6** (2016) 30380.
[33] S. Kajita, T. Nojima, Y. Tomita, N. Ohno, H. Tanaka, N. Yoshida, M. Yajima, T. Akiyama, M. Tokitani and T. Yagi: Surface and Coatings Technology **340** (2018) 86.
[34] Y. Ueda, N. Yamashita, K. Omori, H. Lee, K. Ibano and A. Ito: Journal of Nuclear Materials **511** (2018) 605.
[35] J. Yu, M. Baldwin, R. Doerner, T. Dittmar, A. Hakola, T. Hoschen, J. Likonen, D. Nishijima and H. Toudeshki: Journal of Nuclear Materials **463** (2015) 299.
[36] M. Baldwin and R. Doerner: Journal of Nuclear Materials **404** (2010) 165.
[37] S. Kajita, N. Ohno, M. Yajima and J. Kato: Journal of Nuclear Materials **440** (2013) 55.
[38] G. De Temmerman *et al.*: In proceeding of 23rd PSI conference (2018).
[39] D. Nishijima, M. Baldwin, R. Doerner and J. Yu: Journal of Nuclear Materials **415** (2011) S96.
[40] S. Kajita, Y. Tsuji and N. Ohno: Phys. Lett. A **378** (2014) 2533.
[41] M. Yajima, Y. Hatano, S. Kajita, J. Shi, M. Hara and N. Ohno: Journal of Nuclear Materials **438** (2013) S1142.
[42] D. Hwangbo, S. Kajita, N. Ohno and D. Sinelnikov: IEEE Transactions on Plasma Science **45** (2017) 2080.
[43] E. Dechaumphai, J. L. Barton, J. R. Tesmer, J. Moon, Y. Wang, G. R. Tynan, R. P. Doerner and R. Chen: Journal of Nuclear Materials **455** (2014) 56 .
[44] S. Cui, M. Simmonds, W. Qin, F. Ren, G. R. Tynan, R. P. Doerner and R. Chen: Journal of Nuclear Materials **486** (2017) 267.
[45] S. Kajita, T. Yagi, K. Kobayashi, M. Tokitani and N. Ohno: Results in Physics **6** (2016) 877 .
[46] K. Woller, D. Whyte and G. Wright: Nuclear Fusion **57** (2017) 066005.
[47] D. Hwangbo, S. Kajita, N. Ohno, P. McCarthy, J. W. Bradley and H. Tanaka: Nuclear Fusion **58** (2018) 096022.
[48] S. Kajita, S. Kawaguchi, N. Ohno and N. Yoshida: Sci. Rep. **8** (2018) 56.
[49] S. Kajita, S. Kawaguchi, N. Yoshida, N. Ohno and H. Tanaka: Nuclear Fusion **58** (2018) 106002.
[50] D. Nishijima, Y.Kikuchi, M. Nakatsuka, M. Baldwin, R. Doerner, M. Nagata and Y. Ueda: Fusion Science and Technology **60** (2011) 1447.
[51] S. Barengolts, G. Mesyats and M. Tsventoukh: Nuclear Fusion **50** (2010) 125004.
[52] S. Kajita, N. Ohno, N. Yoshida, R. Yoshihara and S. Takamura: Plasma Physics and Controlled Fusion **54** (2012) 035009.
[53] A. Anders*Cathodic Arcs: From Fractal Spots to Energetic Condensation* (Springer, New York, 2008).
[54] S. Kajita, N. Ohno, Y. Tsuji, H. Tanaka and S. Takamura: J. Phys. Soc. Jpn. **79** (2010) 054501.
[55] S. Kajita, S. Takamura and N. Ohno: Plasma Physics and Controlled Fusion **53** (2011) 074002.
[56] D. Hwangbo, S. Kajita, S. A. Barengolts, M. M. Tsventoukh and N. Ohno: Results in Physics **4** (2014) 33.
[57] D. U. B. Aussems, D. Nishijima, C. Brandt, R. P. Doerner and N. J. L. Cardozo: Journal of Applied Physics **116** (2014) 063301.
[58] D. Hwangbo, S. Kajita, M. Osaka and N. Ohno: Japanese Journal of Applied Physics **52** (2013) 11NC02.
[59] D. Hwangbo, S. Kawaguchi, S. Kajita and N. Ohno: Nuclear Materials and Energy **12** (2017) 386 .
[60] D. Hwangbo, S. Kajita, S. A. Barengolts, M. M. Tsventoukh, S. Kawaguchi, V. G. Mesyats and N. Ohno: Contributions to Plasma Physics **58** (2018) 608.